Carbon 184 (2021) 91–101

Contents lists available at ScienceDirect

Carbon

journal homepage: www.elsevier.com/locate/carbon

Research Article

"Sticky" carbon coating enables high-area-capacity lithium storage of silicon-graphitic carbon hybrid

Zidong Chen [a, b], Lun Li [a, d], Zheng Zhang [a, b], Hao Li [a, b], Bo Xie [c], Yungui Chen [a, b], Ali Davoodi [d, e], Saman Hosseinpour [e, f], Wei Liu [a, b, *]

[a] Institute of New-Energy and Low-Carbon Technology (INELT), Sichuan University, Chengdu, Sichuan, 610065, China
[b] Engineering Research Center of Alternative Energy Materials & Devices, Ministry of Education, Sichuan University, Chengdu, Sichuan, 610065, China
[c] Chengdu Silan Semiconductor Manufacturing Co., LTD, China
[d] Sichuan University - Pittsburgh Institute (SCUPI), Chengdu, Sichuan, China
[e] Materials and Metallurgical Engineering Department, Faculty of Engineering, Ferdowsi University of Mashhad, Mashhad, Iran
[f] Institute of Particle Technology (LFG), Friedrich-Alexander-Universität-Erlangen-Nürnberg (FAU), Cauerstraße 4, 91058, Erlangen, Germany

ARTICLE INFO

Article history:
Received 27 May 2021
Received in revised form
21 July 2021
Accepted 30 July 2021
Available online 5 August 2021

Keywords:
Si anode
Surface moieties
Solid electrolyte interface
High-area capacity
Lithium storage

ABSTRACT

Pulverization and surface instability have been identified as the main impediments to the application of Si anodes in high-energy lithium-ion batteries (LIBs). In this study, a Si-graphitic carbon hybrid (SiG) is created via embedding Si nanoparticles in between expanding graphite interlayers, thus to be adopted as a model system to unravel structure-properties relations for LIBs applications. We explore the impact of artificial surface coating layers on the lithium cycling performance of SiG particles. In comparison with native SiG and carbon-coated SiG (CC-SiG), we find that the "sticky-carbon" coating, i.e., an epoxy-rich layer on top of the carbon coating, gave rise to superior cycle performance. In the "sticky carbon" coated SiG (SCC-SiG), the surface chemistry appears to have a pivotal role in both alleviating electrode disintegration and forming a favorable SEI rich in fluorine-polymers. These positive findings are examined in electrodes with mass loading ranging from 1.0 to 5.0 mg/cm^2, achieving area capacities up to ~5.0 mAh/cm^2. A full cell adopting >6 mg/cm^2 $LiNi_{0.8}Co_{0.1}Mn_{0.1}O_2$ (NCM811) cathode and SCC-SiG delivers stable cycling performances. It is hence unraveled that the carbon coating layer with reactive surface groups on the top is an unrecognized key for wide range of Si-based anodes.

1. Introduction

Lithium-ion batteries LIBs with high energy density and long cycle life have been regarded as essential components in systems like electric vehicles, portable electronics, and stationary grid energy storage, etc. [1] Silicon (Si), as an inherent naturally abundance element, has emerged as a promising anode material for LIBs for it offers a high Li-storage capacity of ~3580 mAh/g (corresponding to $Li_{15}Si_4$) and low working potential (0–0.4 V vs Li/Li). However, it is now well established that the cycle-induced large volume expansion (~300%) of Si is the main obstacle towards its commercial application as the anode in LIBs. Such extensive cycle-induced volume expansion of Si leads to electrode disintegration and solid electrolyte interphase (SEI) overgrowth which are the main culprits for the capacity loss and shortened cycle life of LIBs [2–4].

Carbon coating, carbon host, etc., are often adopted structural designs to ameliorate cycle-induced structure disintegration and loss of electrical contact for anodes with large volume expansion (e.g. Si, Sn, oxides, etc.) [5–8]. Graphene have shown promising advantages for hosting Si due to their superior flexibility and conductivity, making Si-graphene composite an appealing structure in accessing desirable Li-storage reversibility [9–12]. Recently, interactions between binder molecules and the active materials have been drawing increasing attention [13–17]. For instance, it has been shown that the hydro-oxygen groups in the binder polymers like carboxymethyl cellulose (CMC), polyacrylic acid (PAA), alginate, *etc.*, can hydrogen bond with the Si surface to help to suppress the cycle-induced particle pulverization [18–20]. However, these hydro-oxygen groups are also reported to initiate a series of autocatalytic side reactions of electrolyte, giving rise to SEI build-up and impedance increases [21–23]. These negative effects would be

* Corresponding author. Institute of New-Energy and Low-Carbon Technology (INELT), Sichuan University, Chengdu, Sichuan, 610065, China.
E-mail address: weiliu@scu.edu.cn (W. Liu).

https://doi.org/10.1016/j.carbon.2021.07.097
0008-6223/

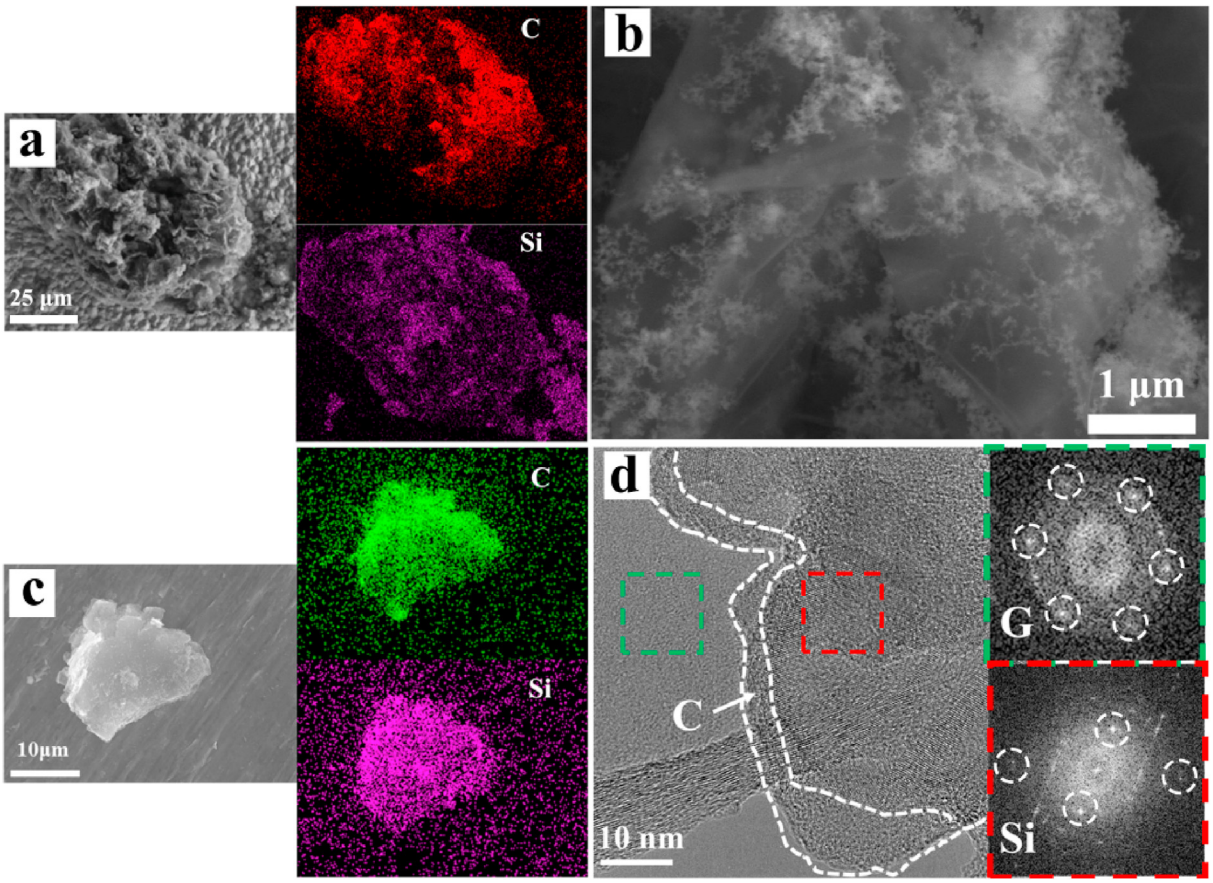

Fig. 1. The formation of a Si-graphitic carbon (SiG) hybrid with ideal host structure. **(a)** SEM micrographs and the corresponding EDS elemental maps of C and Si of one SiG, highlighting the uniform distribution of SiNPs in the expanded graphene host. **(b)** High-resolution SEM image of SiG. **(c)** SEM micrograph and corresponding EDS elemental maps of CC-SiG, depicting a uniform Si–C hybrid particle. (d) High-resolution TEM lattice analysis of a CC-SiG, revealing the crystalline structure Si and graphitic carbon support. The Si particle surface was covered with a layer of amorphous carbon. Insets: fast Fourier transform of the framed area. (A colour version of this figure can be viewed online.)

further amplified at elevated mass loading conditions, with the accelerated gas formation and electrolyte consumption leading to further meltdown of the cell [24]. To date, accessing stable Li cycle performances of high area capacity Si anodes remains challenging.

Prior explorations point to the fact that the surface of the active materials significantly affects many aspects of the electrochemical process in LIBs. It is known that the interactions between the oxide surface of Si/Si–C particles and various binder molecules are important in maintaining electrode structure against volume expansion [3]. Moreover, the surface of silicon and/or carbon directly interfere with the SEI formation so that direct contact of Si with electrolyte is considered detrimental [25,26]. One may find that the role of Si anode particle surface remains non-explicit, as subtle influences from the surface might be masked by relatively low electrode mass loading and excessive active Li supply from the counter electrode. Up to date, mechanistic understanding towards surface chemistry in affecting lithiation/de-lithiation process of Si–C composite particles remains ambiguous, and the design of Si–C hybrid's surface moieties beyond conventional carbon coating is rarely explored. This may however be a critical factor for practical battery applications.

Here we prepare a Si-graphitic carbon hybrid (SiG) with Si nano particles (SiNPs) homogeneously embedded in between expanded graphite inter-galleries via an in-situ chemical-expansion hybridization route. The expanded graphene layers offer superior conductive and mechanical attributes as Si host. This SiG composite was utilized as a model system to unravel the critical role of surface moieties in electrochemical Li-storage reversibility. Three typical types of surface moieties were examined, i.e., native surface, surface with carbon coatings, and with “sticky” carbon coatings. Epoxy reactive groups were introduced onto the topmost layer of carbon coating, creating the “sticky” carbon coating layer. The electrochemical behaviors of the surface-tuned materials were compared and in-depth investigation on the SEI interface and post cycled electrodes morphology were carried out. A profound synergy of fluorine polymer-rich SEI and surface-binder chemical bonding was identified on the sticky carbon-coated surface. This positive effect was examined in both high-area capacity half cell and full cell architectures. XPS and SEM were applied to provide further fundamental insights into the mechanism of surface chemistry in affecting electrode performances.

2. Experimental section

2.1. Materials

Silicon nanoparticles (~50 nm), graphite (1200 mesh), decane, and [γ-(2,3-epoxypropoxy)- propyl]-trimethoxy silane (γ-EPS) were used as-received from Aladdin Chemicals. Sulfuric acid, oleum, n-decane, and ammonium persulfate were supplied by Kelong Chemicals. Carboxymethyl cellulose sodium (CMC), polyacrylic acid (PAA), pitch, and carbon black (CB) were supplied by the Canrd Group.

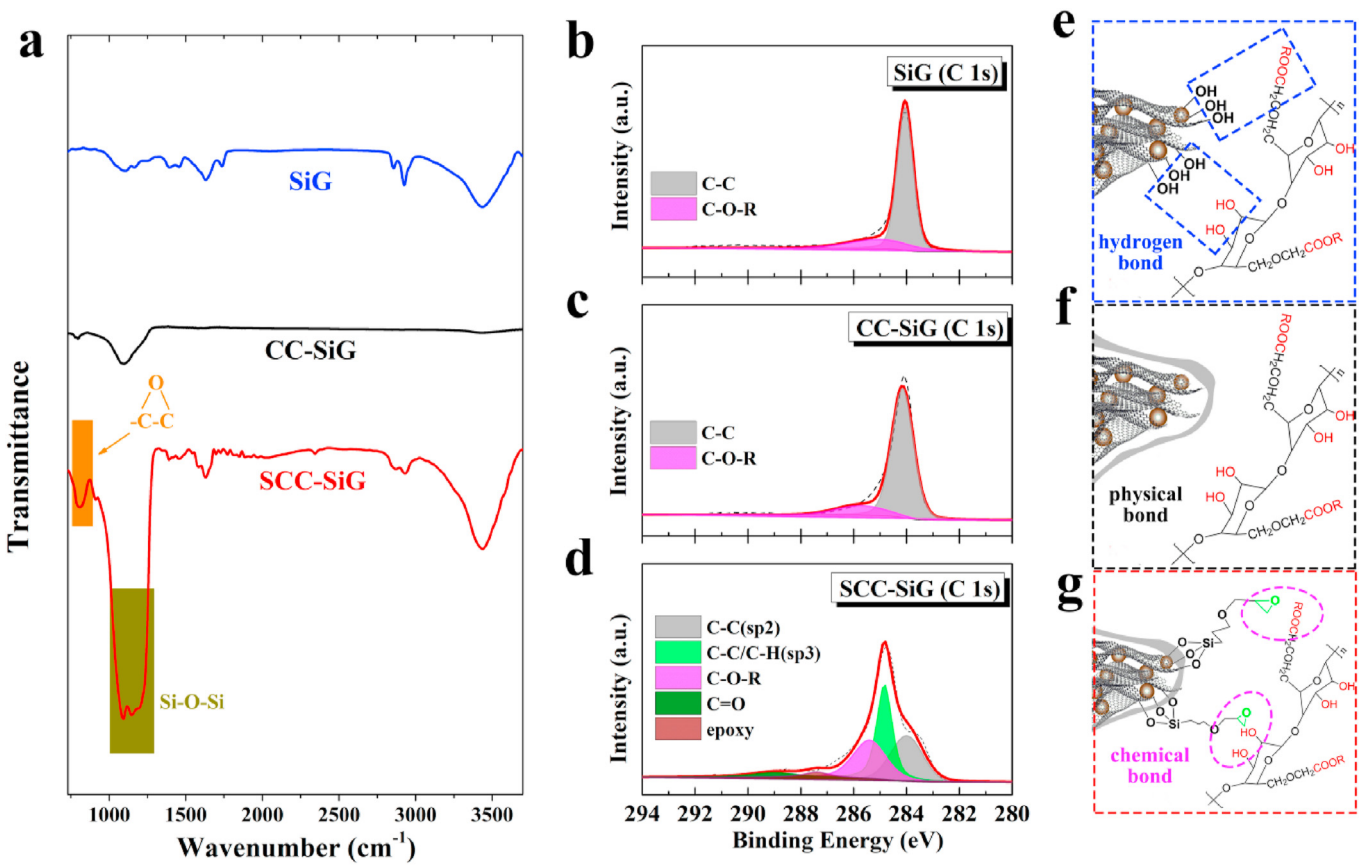

Fig. 2. **(a)** FTIR spectra of SiG, CC-SiG, and SCC-SiG, highlighting the elimination of hydro-oxygen groups from SiG to CC-SiG and introduction of epoxy groups from CC-SiG to SCC-SiG; **(b–d)** XPS C 1s spectra of SiG, CC-SiG, and SCC-SiG respectively, **(e–g)** Schematic illustration of the surface tuned SiG nanocomposite forming varying interactions with the polymer binder molecules. (A colour version of this figure can be viewed online.)

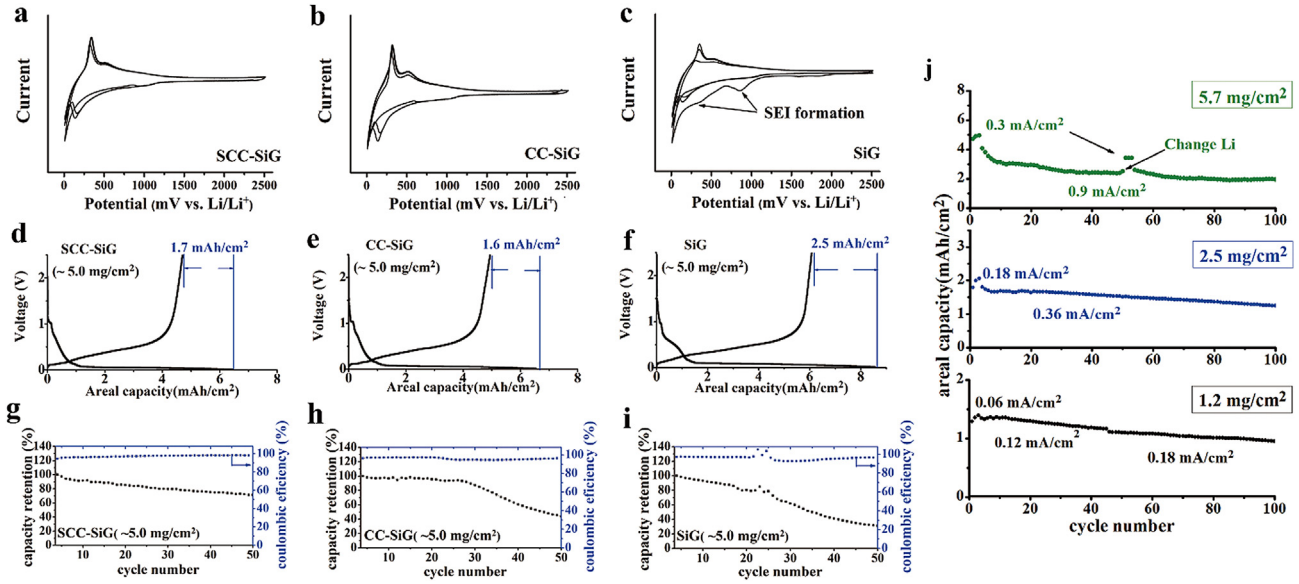

Fig. 3. (a, b, c) Cyclic voltammetry curves of SCC-SiG(a), CC-SiG (b) and SiG(c), tested at 0.1 mV/s; **(d–i)** Initial charge-discharge voltage profile (d–f) and cycling performances (g–i) of SCC-SiG, CC-SiG and SiG, active material mass loading ~5.0 mg/cm^2; **(j)** Cycle performances of SCC-SiG with various mass loading levels. (A colour version of this figure can be viewed online.)

2.2. Synthesis

Liquid-based expansion-hybridization chemistry was employed to expand the interlayer space of graphite that allows Si nanoparticles to flock in, creating a silicon-expanded graphite hybrid with ideal uniformity. In a typical experiment, 98% H_2SO_4 and Oleum were initially mixed in a volume ratio of 4:1 and cooled to room temperature. 6 g of $(NH_4)_2S_2O_8$ was dissolved into 50 mL acid mixture solution and stirred until the salt was completely dissolved. 0.3 g graphite and 0.3 g nano-silicon powder was firstly hand mixed and then step-wise added into the solution. The mixture was transferred to a 60 °C water bath and kept under magnetic stirring overnight. After rinsing with deionized water and centrifugation at the 10000 r.p.m to remove diluted acid, the final product SiG material was obtained by freeze-drying.

Carbon coated SiG hybrid (CC-SiG) was synthesized by modifying the SiG with a layer of carbon. In a typical experiment, commercial pitch and SiG powder in a weight ratio of 1:10 were dissolved in decane under magnetic stirring. Then the uniform solution was transferred into a hot-water bath at 80 °C to allow slow evaporation of decane inside the fume hood. After complete drying, pitch coating on SiG powder was pyrolyzed in a tube furnace under an argon atmosphere. The tube was initially heated to 300 °C for 1 h with a heating rate of 10 °C/min and then further ramped to 900 °C with a heating rate of 5 °C/min and held at 900 °C for 3 h.

"Sticky" carbon-coated SiG hybrid (SCC-SiG) was prepared via a wet-chemistry route where the surface coupling reaction between γ-EPS and CC-SiG was utilized to create a modified surface rich in epoxy moieties. A glacial acetic acid ethanol/aqueous solution (90 vol% ethanol) with a pH ≈ 5.5 was first prepared as a buffer solution. Then γ-EPS was added into the solution in a volume content of 2 vol%. The solution was activated by manual shaking at room temperature for 2 min until a homogeneous solution was obtained. SCC-SiG was obtained by mixing 1.5 mL activated solution with 100 mg CC-SiG powder followed by heating at 80 °C for 1.5 h.

2.3. Analytical characterization

Fourier Transform infrared spectroscopy (FTIR) was performed using a Thermo Scientific Nicolet 7600IR spectrometer. The morphology and structure of the samples were analyzed by Field Emission Scanning Electron Microscopy (FE-SEM, JSM-7500F operated at 15 kV). SEM was equipped with an energy dispersive spectrometer (EDS) mapping (X-Max Extreme, Oxford-Instruments). Transmission electron microscopy was carried out in Tecnai G2-F20, operating at 200 kV. TEM specimens were fabricated by casting a drop of materials dispersion (in isopropanol) onto a lacey carbon copper grid. X-ray photoelectron spectroscopy (XPS) was carried out with ThermoFisher EScalab 250Xi with Al Kα radiation. XPS Peak fitting was performed using Gaussian/Lorentzian peak shapes following subtraction of Shirley's background. X-ray diffraction (XRD) was carried out in a DX2700 instrument (Dandong Haoyuan with Cu Kα radiation). Thermogravimetric analysis (TG) was carried out on Netzsch STA-449 F3 under N_2 atmosphere adopting a heating rate of 10 °C/min.

2.4. Electrochemical Characterization

For slurry preparation, the electrode binders, carboxymethyl cellulose (CMC), and polyacrylic acid (PAA) were pre-dispersed into de-ionized water in a weight ratio of 1:1. Then the obtained active materials were mixed with carbon black (CB) into the viscous CMC/PAA solution in a mass ratio of 8:1:1 (active material: CB: binder) and ground in a mortar to obtain a uniform slurry. Then the slurry was blade-coated on porous nickel mesh with various active material mass loading ranging from 1 to 5 mg/cm^2. Nickel mesh was used as current collectors to facilitate the fabrication of high-area-capacity electrodes. Unlike conventional Cu foil, porous Ni-mesh ensures good electron transport and electrolyte penetration even with the heavy loading of active materials. By avoiding these possible variables, an exclusive correlation between the electrode performances and surface chemistry of SiG can be established. The electrodes were vacuum dried at 60 °C and then roll-compressed into ~200 μm thick discs. Then an annealing step at 120 °C for 24 h under vacuum was adopted to facilitate the surface interactions between the active material and CMC/PAA binder. The dried electrodes were assembled into 2025-type coin cells in an argon-filled glovebox with oxygen and moisture content lower than 0.1 ppm. Celgard 2400 membrane was employed as a separator and a 0.4 mm lithium foil (China Energy Lithium Co., Ltd) was used as a counter electrode in the half-cells. 1 M $LiPF_6$ dissolved in a 1:1:1 (volume ratio) mixture of ethylene carbonate (EC), ethyl methyl carbonate (EMC), and diethyl carbonate (DEC) with 10 vol% fluoroethylene carbonate (FEC) was used as the electrolyte. Approximately 160 μl electrolyte was used for each cell. The galvanostatic charge-discharge cycling tests were performed on LAND-CT2001A battery tester at 0.01–2.5 V vs. Li/Li$^+$. Cyclic Voltammetry (CV) tests were carried out using AUTOLAB M204 (Metrohm, Switzerland), operating at 0.1 mV/s. Nickel-rich layered oxide cathodes were prepared by mixing NCM811 powder with polyvinylidene-difluoride (PVDF) and CB in N-Methyl pyrrolidone (NMP) with a weight ratio of 8:1:1 and coated the slurry on aluminum foil with active material mass loading of ~6.4 mg/cm^2. The capacity ratio of the anode to cathode (N/P ratio) was controlled at ~1.3. The anode electrodes were preconditioned in half cells for a few cycles and then assembled into the full cell. Full cells were firstly cycled at 0.1 C–0.1C charge-discharge after which higher currents were adopted. Cycling C-rate was defined by cathode area capacity (1C = 1.2 mAh/cm^2). Post-cycled electrodes were extracted from cycled cells and then repeatedly rinsed in the glove box with dimethyl carbonate (DMC) to remove residual electrolyte.

3. Result and discussion

Incorporating Si nanoparticles (SiNPs) into a Si-carbon hybrid structure, i.e. carbon coating, carbon support, etc., is a known strategy to access superior lithium storage performance [9,12,27]. Here we prepare a Si-graphitic carbon hybrid structure with SiNPs uniformly embedded in between expanded graphene layers, providing a Si–C hybrid model system for further investigations. An in-situ expansion-hybridization method was adopted to obtain such structure. After immersion in the expansion agent ($(NH_4)_2S_2O_8/H_2SO_4$/oleum mixture), the interlayered structure of graphite will greatly expand [28]. Co-adding the SiNPs and graphite into the reacting agent results in uniform SiNPs adsorption onto the newly exposed graphene surfaces, obtaining an ideally dispersed Si-graphitic carbon (SiG) hybrid. After repeated rinsing, a freeze-dried SiG nanocomposite material was obtained.

Fig. 1a shows the SEM micrograph and the corresponding EDS elemental mapping of C, Si of a dry-state SiG particle that was deposited on the Ni substate. The uniform distribution of Si and C signals within the particle indicates the formation of a homogeneous SiG hybrid. The high-resolution SEM image shown in Fig. 1b further confirms the successful introduction of SiNPs into the interlayer space of the expanded graphite host. XRD patterns (Fig. S1) indicate the greatly expanded and exfoliated (002) interlayer spacing of graphite into expanded graphene, allowing the in-situ loading of a large amount of SiNPs with Si:C ratio up to 1:1.

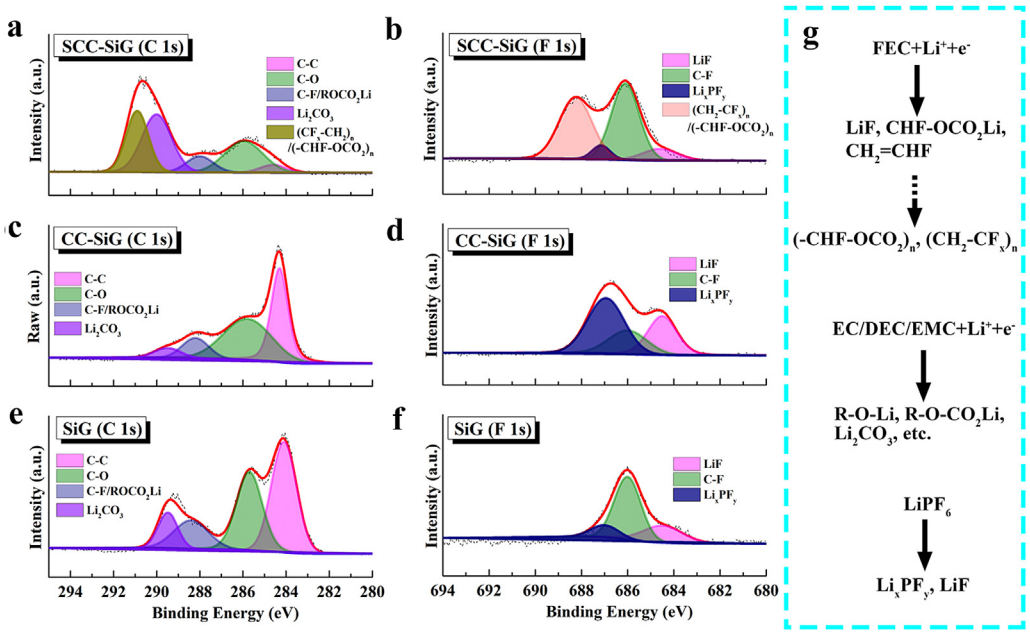

Fig. 4. XPS C 1s **(a, c, e)** and F 1s spectra **(b, d, f)** of post cycled electrodes, highlighting the differences of surface moieties in affecting the SEI film composition in SCC-SiG **(a, b)**, CC-SiG **(c, d)** and SiG **(e, f)**. (g) Illustration of SEI compounds derived from various electrolyte components and reaction routes. (A colour version of this figure can be viewed online.)

Raman spectrum of the SiG material (Fig. S2) shows a strong peak at 516 cm^{-1}, suggesting high crystallinity of Si in good agreement with high-resolution TEM (HR-TEM) lattice analysis and XRD patterns. Moreover, graphitic carbon 2D peak and G peak at 2715 and 1580 cm^{-1} were also observed in the Raman spectrum. The high Raman G:D ratio (I_G:I_D = 12.1) indicates the highly ordered and ultra-low defect nature of the graphene layers. It should be noted that traditional reduced graphene oxide (r-GO) usually has an I_G:I_D of ~0.5–1 [29]. The graphitic carbon supports with lower defect contents are reported to give superior electrical conductivity and compatibility with electrolyte [30], making the SiG material an ideal model system to study the role of surface moieties in electrochemical cycling. As will be elucidated in later discussion, the surface of SiNPs in protogenic SiG is rich in oxygen groups.

Previous studies showed that the surface oxide layer in Si is beneficial in improving the cycle performance of Si, assumably due to the hydrogen bonding with binder molecules [13,18,20]. However, two aspects of surface interactions call for attention when dealing with surface oxygen groups: (1) the hydrogen bonding is sensitive and fragile at varying electrochemical potentials and/or at large strain levels, (2) the protic hydroxyl groups promote electrolyte decomposition and SEI instabilities via series of autocatalytic side reactions [22,31]. Conversely, carbon coating gives rise to improved cycle performances of Si particles via isolating electrolyte side-reactions [32–35]. As the mechanistic interdependence between Si surface and electrochemical lithium cycling behavior remains ambiguous, subtle influences from electrode mass loading and current densities may further give rise to diverged understanding of ideal surface chemistry [36]. We propose that further investigations on the mechanical and chemical impact of surface chemistry of Si–C particles are seminal.

Hence, we adopt the as-prepared SiG as a baseline material and synthesized a series of surface structures and compared them in parallel as: (1) the protogenic surface of neat SiG, which is rich in protic oxygen groups, (2) a carbonaceous surface via coating a layer of carbon onto SiG, and (3) a “sticky” carbon-coated surface via further attaching organo-silane functional groups on top of the carbon-coated SiG. To prepare carbon-coated SiG (denoted CC-SiG), a layer of pitch was liquid phase coated onto SiG and then the material was subject to pyrolysis at 900 °C. This process generates a layer of simple substance carbon covering the protogenic surface. Fig. 1c shows the SEM and the corresponding EDS elemental mapping image of CC-SiG, highlighting the uniform distribution of Si and C elements. HRTEM analysis of CC-SiG is shown in Fig. 1d, demonstrating the crystalline nature of a typical Si nanoparticle loaded on the graphitic carbon layer. The corresponding fast Fourier transform (FFT) pattern further confirms the (111) and (200) crystallographic planes of the face-centered cubic (fcc) form of Si (red frame), and (100) crystallographic planes of hexagonal graphene (green frame). The amorphous carbon layer about 5–10 nm in thickness on the surface of SiNPs is also clearly observed in this image. The crystalline nature of SiNPs and expanded graphitic carbon layer were not altered after pitch carbon coating, as characterized by XRD shown in Fig. S1.

To prepare the “sticky” carbon surface, we further grafted epoxy moieties onto the carbon coating layer of CC-SiG. A deliberate mild reaction (80 °C at 1.5h) of SCC-SiG with γ-EPS was utilized to trigger the surface coupling reaction, yielding a surface that is rich in epoxy groups on top of the carbon coating layer. The “sticky” carbon layer could isolate electrolyte side reactions similar to conventional carbon coatings. Moreover, the “sticky carbon layer” is chemically reactive with CMC/PAA binder via epoxy ring-opening reaction during electrode drying whilst the carbon coating layer is inert with the binder. This “sticky” carbon-coated SiG nanocomposite is denoted as SCC-SiG, hereafter. The dosage of surface modifiers, i.e. γ-EPS, was elaborately controlled to a minor amount to minimize the variation of weight percentages of active material. According to TG results (Fig. S3), the epoxy-silane molecules attached in SCC-SiG account for ~5 wt% of the composite.

The FTIR spectra of SiG, CC-SiG, and SCC-SiG are shown in Fig. 2a. As can be seen in these spectra, the SiG exhibits quite strong adsorption at ~3400 cm^{-1} that corresponds to the stretching vibration of –OH groups. Indeed, SiG is rich in surface oxygen groups. In CC-SiG, the –OH absorption becomes much weaker suggesting the elimination of –OH surface groups during high-temperature pyrolysis. The characteristic absorption of epoxy groups was

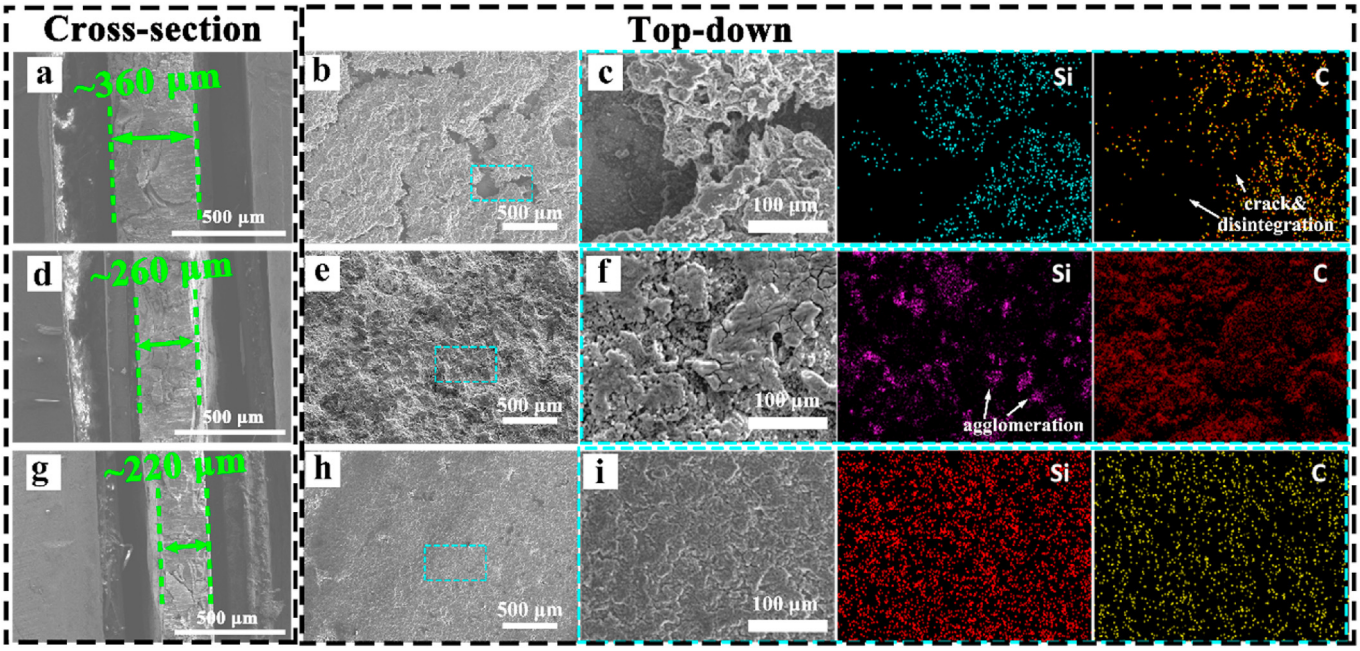

Fig. 5. SEM and EDS analysis on post-cycled electrodes of SiG(a-c), CC-SiG(d-f), and SCC-SiG (g–i). (a, d, g) Cross-section SEM images of post-cycled electrodes of SiG (a), CC-SiG (d), and SCC-SiG (g), Ar^+ ionic mill was employed to process the electrodes' cross-section; (b, e, h) Top-down SEM images of post-cycled electrodes of SiG (b), CC-SiG (e) and SCC-SiG (h); c, f, and i are higher magnification images and corresponding EDS Si and C elemental maps of framed area in b, e, and h, respectively. (A colour version of this figure can be viewed online.)

observed in SCC-SiG at ~908 cm^{-1}, indicating the formation of an epoxy-rich reactive surface. This is further verified in TG results as a notable weight loss at 350 °C in SCC-SiG, which corresponds to the removal of attached γ-EPS modifiers (Fig. S3). The −OH absorption at ~3400 cm^{-1} in SCC-SiG was attributed to the residual water/ethanol after a deliberate mild reaction (80 °C at 1.5 h) of SCC-SiG with γ-EPS. We here underline the elaborate implementation of reaction-drying temperature (80 °C) as higher temperatures make the reactive epoxy groups unstable. Annealing of SCC-SiG electrodes at 120 °C under vacuum (detailed in experimental section) could trigger epoxy-binder bridging reactions and thoroughly remove remnant H_2O and ethanol molecules. Fig. 2 b, c, and d display the XPS C 1s spectra of SiG, CC-SiG, and SCC-SiG respectively. The C 1s spectrum of SiG exhibits a major peak at 284.1 eV that is typical for sp^2 hybridized C–C bonds in expanded graphene layers. The C–O group peak at 285.6 eV is minor in SiG [37–39]. Both XPS C 1s spectra and Raman results point to the fact that the oxygen groups predominantly exist on the Si surface while being minimal on the expanded graphitic carbon host. While the CC-SiG shows C 1s spectra similar to SiG with predominant sp^2 C–C and C–O-R peaks, the SCC-SiG displays rather noticeable peaks at 284.8 eV and 287.2 eV that are ascribable to sp^3 C–C/C–H (alkyl chains) and epoxy groups, respectively [40,41]. These peaks are evidence of the existence of attached γ-EPS molecules on the surface. Fig. 2 e, f, and g schematically illustrate the surface structures of SiG, CC-SiG, and SCC-SiG and the associated interfacial interactions between active materials and polymer binder molecules, respectively. Neat SiG is rich in surface hydroxyl groups that can interact with polymer binder molecules via hydrogen bonding (Fig. 2e). In CC-SiG, the surface hydroxyl groups were replaced with a layer of carbon coating, generating surfaces that only have physical interaction with the polymer binder (Fig. 2f). Conversely, SCC-SiG can form covalent bridges with polymer binder molecules via epoxy ring-opening reaction (Fig. 2g). Hereinafter, SiG, CC-SiG, and SCC-SiG will be utilized to elucidate the role of surface chemistry in determining battery performances.

CV curves of SCC-SiG, CC-SiG, and SiG are shown in Fig. 3 a, b, and c respectively. In the initial sweep of SiG, we observed quite discernible cathodic peaks at 800 and 500 mV vs. Li/Li^+ in SiG, which were assigned to the electrolyte decomposition on the SiG surface to form SEI film. It may be concluded that the protogenic surface of SiG catalyzes electrolyte decomposition which leads to excessive SEI formation that causes electrolyte consumption and loss of active lithium. In CC-SiG and SCC-SiG, these SEI-related signals are indiscernible. As surface coating imposes little changes to materials' surface area, we believe the surface area of the three groups should be on-pair. Therefore, an intrinsic isolation-passivation effect can be confirmed from carbon and "sticky carbon" coated surfaces in CC-SiG and SCC-SiG. In SiG, the overgrowth of SEI is indicative of unremitting parasitic side reactions of electrolyte on the electrode surface, leading to gas formation and continuous polarization growth. The differing electrolyte side reactions are usually associated with initial cycle capacity loss [21–23]. The galvanostatic charge-discharge performances of SiG, CC-SiG, and SCC-SiG were compared with standard electrode mass loadings of ~1.0 mg/cm^2 as shown in Fig. S4. All three groups exhibit stable lithiation/de-lithiation voltage profiles at 0.06 mA/cm^2. SiG exhibits the most severe initial cycle loss among all samples, being ~600 mAh/g, much higher than that of CC-SiG and SCC-SiG (both ~350 mAh/h). These results reverberate with the CV results shown in Fig. 3 a-c, indicating severe electrolyte decomposition and excessive SEI formation on the protic surface of SiG. Here we demonstrate that modifying the materials with either carbon or "sticky carbon" layer are both effective in stabilizing the SEI interface in the initial lithiation step. Examining repeated lithiation/de-lithiation cycles of 20 cycles (Fig. S4 d, e, and f), SCC-SiG exhibits capacity of 1051.0 mAh/g with a capacity retentions of 94.7%, slightly higher than that in CC-SiG (~846.4 mAh/g and 80.3% retention) and SiG (~979.7 mAh/g and 83.6% retention). These values correspond to area capacities of ~1.3, ~1.0, and ~1.1 mAh/

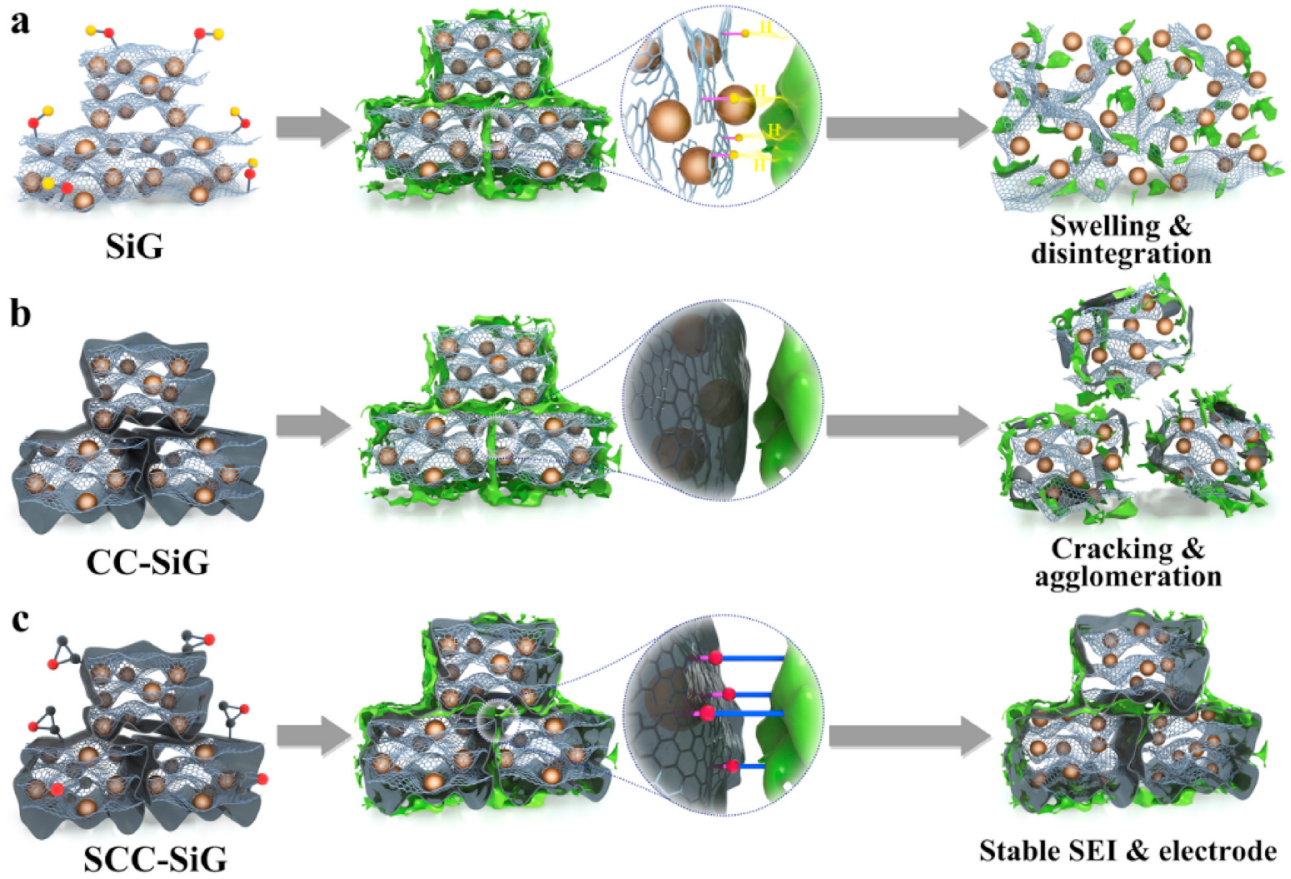

Fig. 6. Schematic summary of surface structure and its critical role in affecting electrochemical performances of SiG with hydroxyl surface **(a)**, CC-SiG with simplex carbon coating **(b),** and SCC-SiG with "stick" carbon coating **(c)**. During cycling, the hydroxyl surface promotes electrolyte decomposition and electrode cracking; carbon coating isolates electrolyte side reactions however electrode cracking persists due to lack of particle-binder adhesion; "sticky" carbon layer reinforces active material – binder interactions and promotes the formation of an SEI with superior stability. (A colour version of this figure can be viewed online.)

cm^2, respectively. The slightly higher capacity in SiG can be attributed to its oxygen groups serving as extra lithium storage sites. However, given the low mass loading level of active materials (~1 mg/cm^2), the ample supply of active Li and electrolyte may mask the interfacial instability issue in SiG, leading to seemingly on-pair capacity fading rates of SiG and CC-SiG. In contrast, SCC-SiG achieved relatively higher capacity retention than its counterparts. It can be proposed that the electrochemical performances in lower mass loading electrodes are somewhat elusive and the key factors may only be captured by increasing the mass loading levels of electrodes.

The electrode area capacity in commercial Li-ion cells ranges from 3 to 5 mAh/cm^2. Accordingly, we examined the electrochemical behaviors in electrodes with higher mass loading levels (~5.0 mg/cm^2). Fig. 3 d, e, and f show the initial charge-discharge profile of high-mass-loading electrodes of SCC-SiG, CC-SiG, and SiG, displaying area capacities of 4.7, 4.9, and 6.1 mAh/cm^2 at the current density of 0.3 mA/cm^2, respectively. The slightly higher capacity in SiG is consistent with previous studies that the oxygen groups can act as additional lithium storage sites [42,43]. Moreover, the remarkable difference lies in SEI-related initial capacity loss. We observed initial capacity loss of 1.7, 1.6, and 2.5 mAh/cm^2 for SCC-SiG, CC-SiG, and SiG, respectively. This phenomenon demonstrates the tremendous impact of surface chemistry on SEI-related capacity loss. Considering the fact that for all tested groups the Si-carbon content and active material fraction are identical, the SEI formation propensity and the associated early cycle capacity loss can be directly ascribed to the differing surface moieties on tested samples. In Fig. 3 g-i the extended cycling performances at an elevated current density of 0.6 mA/cm^2 are shown after three activation cycles. Electrode capacities were all normalized accordingto their initial capacities at identical current densities. It is generally perceived that the cycle stability of Si-based anodes is predominately affected by its capability to endure the ~300% volume change and particle pulverization. As can be observed in Fig. 3i, SiG exhibits the most severe capacity decay among studied samples. SiG retained only 31.1% of its capacity after 50 cycles. In CC-SiG, cycle stability was improved in the initial 20 cycles, however, fast capacity decay (a "rollover" type failure) emerged in the following cycles. After 50 cycles, capacity retention of 43.9% was maintained (Fig. 3h). This "rollover" type capacity failure was previously identified to be associated with accelerated SEI build-up and electrolyte dry-out [44]. We suspect that after repeated volume expansion, electrode disintegration and particle cracking in CC-SiG may have led to the exposure of larger areas of fresh surface that further accelerates capacity fade. Conversely, SCC-SiG exhibits much-improved cycling behavior, delivering 71.5% capacity retention at the 50th cycle.

It may also be noticed that the SiG, CC-SiG, and SCC-SiG exhibit somewhat on-pair cycle performances in low-mass electrodes. However, their electrochemical performances in high-mass electrodes diverge substantially. We deduce that the differing electrochemical behavior in high-mass electrodes can be attributed to both surface instabilities and durability against volume change, as

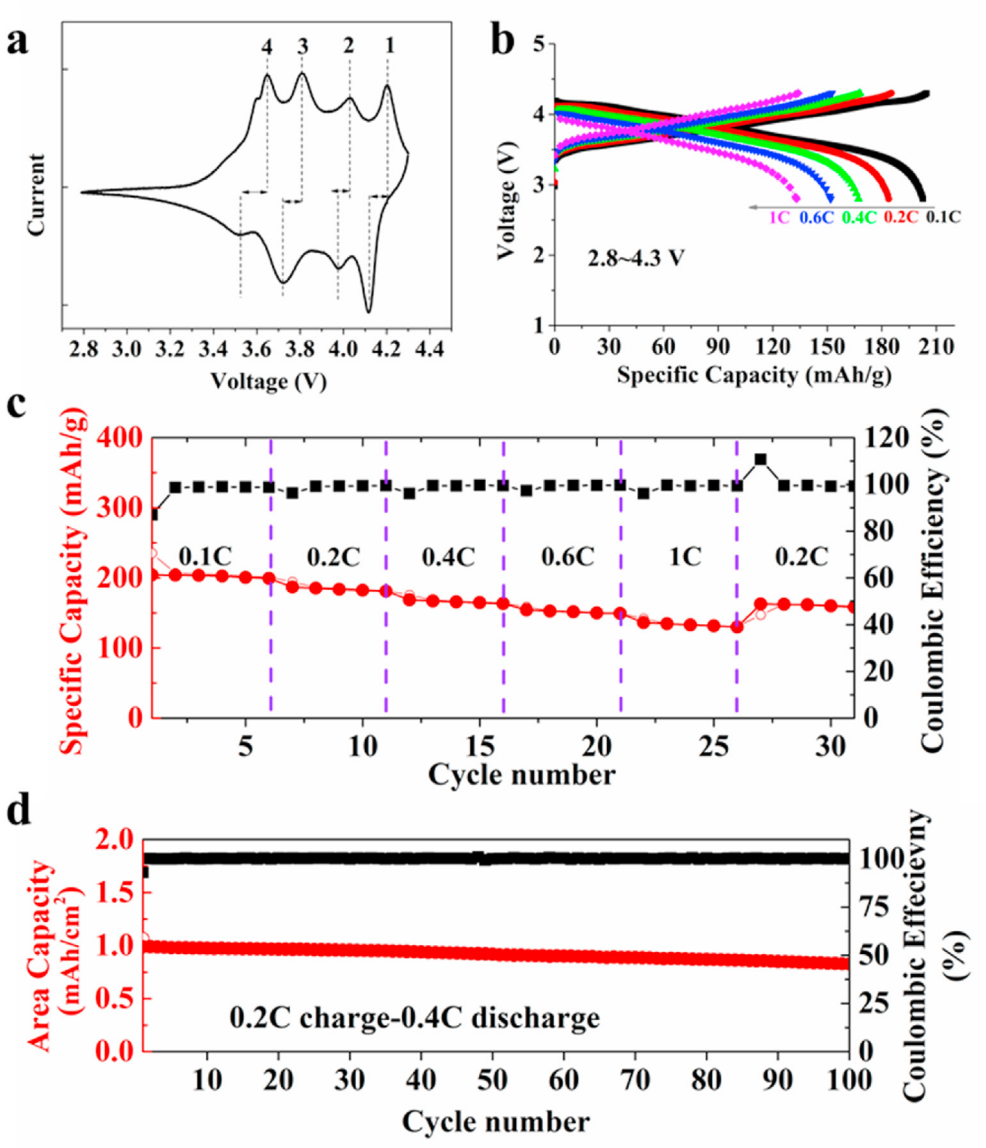

Fig. 7. Full cell performances adopting SCC-SiG anode and NCM 811 cathode. **(a)** cyclic voltammetry (CV) curves ranging from 2.8–4.3 V at 0.2 mV/s, showing 4 highly reversible redox peak pairs. **(b)** Full cell charge-discharge voltage profiles at various C-rate conditions. **(c)** Device capacity and CE as a function of C rate. **(d)** Extended cycling profile of full cell, highlighting stable area capacity and CE during extended cycling. 1C = 1.2 mA/cm.^{2}.

electrode disintegration and electrolyte consumption can be greatly amplified at higher mass loading conditions. At lower mass electrodes, these influences might be masked by the relatively ample supply of electrolyte and active Li. SCC-SiG electrodes simultaneously exhibit improved surface stability and adhesion with the binder. Hence, SCC-SiG electrodes can deliver stable capacities of 1.4, 2.1, and 5.0 mAh/cm^2 upon increasing the mass loading level from 1.2 to 2.5 and 5.7 mg/cm^2, respectively (Fig. 3j). The 1.2 and 2.5 mg/cm^2 electrodes deliver capacity retention of 85.5% (0.9 mAh/cm^2) and 69.1% (1.3 mAh/cm^2) after 100 cycles at elevated current densities. We found that for higher mass loading electrodes the capacity was affected by the Li-metal counter electrode. As shown in Fig. S5, cycling at high-capacity conditions greatly promotes dendrites and "dead" Li formation on the Li metal side. After replacing Li metal counter electrode, the capacity of 5.7 mg/cm^2 SCC-SiG recovered to 3.4 mAh/cm^2 at 0.3 mA/cm^2 at cycle 51st (68% retention) and gave rise to another stable 50 cycles at 0.9 mA/cm^2. The strong particle-binder connection as well as a stabilized electrode surface in SCC-SiG prevented pre-mature failure that is prevalent in SiG and CC-SiG and enabled superior cycle life of electrodes at commercial level area capacities.

Fig. 4 presents the XPS analysis of post-cycled electrodes in their de-lithiated state. Fig. 4 a, c, and **e** compares the C 1s spectra for the post cycled SiG, CC-SiG, and SCC-SiG electrodes, respectively. Several SEI components are identified from C 1s spectra in SiG and CC-SiG; mainly Li_2CO_3 (289.8 eV), C—F/$ROCO_2Li$ (288.4 eV), and C—O (285.6 eV) species. A profound peak at 291 eV emerged in the SCC-SiG sample. This peak corresponds to oligomer/polymeric $(CHF—OCO_2)_n/(CF_x\text{-}CH_2)_n$ species and is found in neither SiG nor CC-SiG. Based on the F 1s spectra shown in Fig. 4 b, d, and **f**, SEI components of Li_xPF_y (687.1 eV), C—F (686.1 eV), and LiF (684.4 eV) are identified in post-cycled SiG and CC-SiG electrodes. Conversely, a profound $(CHF—OCO_2)_n/(CF_x\text{-}CH_2)_n$ peak at 688.3 eV showed up in post-cycled SCC-SiG. From the F 1s spectra of post-cycled SiG and CC-SiG, the F-containing polymeric SEI component in 688.3eV is absent.

Fig. 4g depicts the surface passivation reactions of the organic electrolyte on the electrode surface, resulting in the formation of various SEI compounds. FEC, as a key electrolyte component used in the current study, has a relatively higher LUMO (lowest unoccupied molecular orbital) compared to that of EC, DEC, and EMC, etc. Hence, FEC has the strongest reactivity toward reduction and will firstly decompose on the electrode surface via ring-opening and decarboxylation reaction routes, resulting in the formation of LiF and F-containing organic C–F compounds (e.g. CHF–CH_2, –CHF-OCO_2-). Further ripening of these products gives rise to highly elastic and chemically stable polymeric species such as $(CHF–OCO_2)_n$ and $(CF_x\text{-}CH_2)_n$ [45,46]. In general, $LiPF_6$ and carbonate solvents (EC/DEC/EMC) start to decompose after FEC decomposition, generating SEI layer which consists of Li_xPF_y, LiF, RO-Li, $ROCO_2Li$ and Li_2CO_3, etc. It is known that lithium alkoxide (ROLi) and lithium oxydate alkyl carbonates ($ROCO_2Li$) are mainly the decomposition products of carbonate solvents [47,48]. Therefore, the relatively higher content of ROLi and $ROCO_2Li$ in SiG points to the catalyzed decomposition of carbonate electrolyte solvents in SiG. Accordingly, the general pattern of SEI formation on the varying surfaces may be qualitatively concluded as: (1) the protogenic hydroxyl-rich surface in SiG is catalytic towards carbonate solvent (FEC and EC/DEC/EMC) decomposition, generating an SEI layer rich in $ROCO_2Li$, Li_2CO_3, and C–F species. The unremitting decomposition of electrolytes hinders the polymerizing and crosslinking reactions hence elastic and stable F-polymeric species could not form; (2) the carbon coating layer in CC-SiG suppresses decomposition of carbonates, leading to higher content of Li_xPF_y and LiF species from $LiPF_6$ decomposition; (3) In SCC-SiG, the "sticky" carbon coating layer with γ-EPS groups on the topmost surface suppresses decomposition of both EC/DEC/EMC carbonates and $LiPF_6$ salt, promoting the generation of an F-rich SEI layer. This SEI layer mainly consists of LiF, polycarbonates $(CHF–OCO_2)_n$ and polyfluorovinylene $(CF_x\text{-}CH_2)_n$ and is formed predominately by accumulation and later-on ripening of FEC decomposition products [49–51].

It is known that the polymeric compounds are desirable SEI components for Si anodes, offering excellent flexibility that helps to accommodate volume changes [45]. Moreover, these polymers can further de-fluorinate and generate interior radicals to produce a cross-linked network. The formation of such a cross-linked network further stabilizes the SEI layer to maintain its chemical and structural attributes during prolonged cycling [50]. The relatively higher content of $(CHF–OCO_2)_n$, $(CF_x\text{-}CH_2)_n$ and C–F species in the SEI of SCC-SiG plays a key role in establishing a stable electrode-electrolyte interface. Conversely, the enrichment of Li_xPF_y, $ROCO_2Li$, and Li_2CO_3 in the SEI layer of SiG and CC-SiG suggests that the interface was not stable and follow-up decomposition of carbonate electrolyte ($LiPF_6$+EC/DEC/EMC) occurred in later stage cycling. We concluded that "sticky" carbon surface in SCC-SiG promotes the formation and crosslinking of polymeric SEI components in the early cycles. The crosslinking of polycarbonates and polyfluorovinylene in FEC-derived SEI is in consistent with prior reports [49,50,52]. Being resistant against prolonged cycling, this polymeric SEI layer in SCC-SiG is associated with by far the most stable lithiaion/de-lithiation behaviors.

The cycle stability of the silicon-carbon composite electrodes is strongly dependent on the capability to endure electrode disintegration and pulverization that result from ~300% volume expansion/contraction from $Si \leftrightarrow Li_{15}Si_4$ reaction**.** Fig. 5 **a, d, and g** compare the cross-section SEM images of the post-cycled electrodes with high mass loading (5 mg/cm^2). The role of carbon coating and "sticky" carbon coating in improving electrode durability versus cycling may be understood by comparing the cross-section morphologies of SiG (Fig. 5a) with that of CC-SiG (Fig. 5d) and SCC-SiG (Fig. 5g). The fresh electrodes were 200 μm in thickness before cycling. It may be observed that cycle-induced electrode swelling and cracking is most severe in SiG, showing ~180% thickness expansion with respect to its original state. For CC-SiG and SCC-SiG, the cycled electrodes displayed alleviated thickness expansion of ~130% and ~110%, respectively. SCC-SiG showed more compact electrode cross-section structure as compared to the other two counterparts. This is further supported by careful examination of the electrodes' cross-section with higher magnification (Fig. S6).

The top-down SEM morphologies and corresponding EDS analysis of post-cycled SiG, CC-SiG, and, SCC-SiG are shown in **Fig. 5 b-c, e-f, and h-i,** respectively. The cycling-induced electrode disintegration was most severe in SiG. Higher magnification images and EDS elemental mapping (Fig. 5 c) reveal that the cracking had led to "peel-off" of active material. This phenomenon explains the electrochemical behavior of SiG, as both excessive SEI formation and disconnection of electrical contact account for fast capacity decay and polarization growth. There could also be a vicious loop: a catalytic surface promoting SEI instabilities and gas formation could exacerbate electrode mud-cracking, which generates more fresh SEI interface to grow in return. Post cycled CC-SiG displayed suppressed electrode disintegration (Fig. 5e). However, in enlarged SEM images and EDS elemental mapping **(Fig. 5f)**, prevailing Si aggregations may be observed. We suggest that the rupture of particle-binder adhesion under volume changes leads to dislocation and agglomeration of Si nanoparticles during cycling. In the lack of proper binding force to anchor the active materials, the Si particles are inclined to migrate and aggregate in response to volume changes. The observed cycle-induced aggregation and cracking are in agreement with previous studies on large-volume-expansion anodes [53,54]. Concomitant electrolyte drying and increase of ion-diffusion barrier can be expected in high-mass CC-SiG, explaining the rollover failure of capacity fade. In contrast, the post-cycled SCC-SiG showed an intact electrode structure that is free of fracture, as can be seen in Fig. 5 h-i. Based on the EDS mapping analysis shown in Fig. 5i, the uniform distribution of Si and C elements on post-cycled SCC-SiG depicts an intact electrode structure that is agglomerate-free. These results highlight the key role of covalent bonding between the active material and polymer binder in suppressing particle pulverization and electrode disintegration. The reactive epoxy groups on the surface of SCC-SiG chemically react with the hydroxyl groups in PAA/CMC binder via epoxy ring-opening reaction during electrode drying, generating Si–O–Si–C chemical bridges between the active material and binder molecules. As chemical bonds (200–400 kJ/mol) have orders of magnitude higher bonding energy than physical bonds (<10 kJ/mol) and hydrogen bonds (20–40 kJ/mol), active material immobilization and improved tenacity against mechanical cracking can be expected in SCC-SiG over CC-SiG and SiG.

Fig. 6 schematically summarizes the role of surface moieties in affecting the structural responses of the electrodes to cycling. The hydrogen bonds between SiG and binder molecules are prone to breaking under the cycle-induced strain. Hydrogen bonds could also "dissolve" during lithiation [25,55]. As schematized in Fig. 6a, the unrecoverable breaking of the hydrogen bonding network leads to severe electrode disintegration, exposing fresh catalytic surfaces and exacerbating SEI overgrowth which in return promotes further cracking. The pitch carbon coating in CC-SiG isolates the active materials from electrolyte corrosion, thus decomposition of carbonate electrolyte is inhibited. However, with a lack of proper "anchoring" force with the polymer binder, the prolonged expansion-contraction cycling gives rise to agglomeration and cracking. This is depicted in Fig. 6b. Causing accelerated electrolyte exhaustion and further build-up of SEI, this is extremely detrimental in high mass loading electrodes. Conversely, in SCC-SiG, the

positive role of "sticky" carbon surface could be understood as two-fold: it promotes the formation of F-polymer and LiF rich SEI layer with superior durability, and it also forms strong chemical bonding with the polymer binders to immobilize the active materials against cycle induced cracking/agglomerating, all of which are demonstrated in Fig. 6c. The chemically and mechanically stable surface of SCC-SiG plays a predominant role in enabling superior lithiation/de-lithiation cycling. In high mass loading electrodes, the above discussed mechanical-electrochemical surface interactions are further amplified, leading to more diverging electrochemical performances.

Fig. 7a shows the CV curves of a full cell pairing SCC-SiG anode against nickel-rich layered oxide cathode ($LiNi_{0.8}Co_{0.1}Mn_{0.1}O_2$, NCM811). Cathode mass loading was ~6.5 mg/cm^2 with N:P ratio of ~1.3. A pre-lithiation step was adopted for SCC-SiG to form a stable SEI and compensate for the possible initial capacity loss [56]. In Fig. 7a, four anodic/cathodic peak pairs can be observed at 4.20/4.12 V, 4.03/3.98 V, 3.80/3.73 V, and 3.64/3.52 V. These anodic/cathodic peak pairs are denoted as peak pair I, II, III, and IV, respectively. It is well known that the NCM811 cathode undergoes two groups of reactions during lithium insertion and de-insertion: Co^{3+}/Co^{4+} redox reaction at ~4.3V vs. Li/Li$^+$, and $Ni^{2+}/Ni^{3+}/Ni^{4+}$ at ~3.8 V vs. Li/Li$^+$ [57]. Hence, the peak pairs of I, II, III, and IV can be attributed to the reversible Li-ion shuttling reaction pairs of $Co^{3+}/Co^{4+}||C/LiC_x$, $Co^{3+}/Co^{4+}||Si/Li_xSi_y$, $Ni^{2+}/Ni^{3+}/Ni^{4+}||C/LiC_x$, and $Ni^{2+}/Ni^{3+}/Ni^{4+}||Si/Li_xSi_y$, respectively. The low potential polarization between oxidation and reduction peaks, i.e. ~79, 50, 70, 120 mV for peak pair I, II, III, and IV, respectively, are indicative of the reversible electrochemical process on both anode and cathode sides.

Fig. 7b overlays the full cell galvanostatic charge-discharge voltage profile at various current densities. At these current density conditions, averaged working potentials of 3.79, 3.77, 3.73, 3.68, and 3.59 V were observed. As shown in Fig. 7c, the full cell delivered a reversible capacity of 200.1, 183.8, 165.7, 152.8, and 133.1 mAh/g at 0.1, 0.2, 0.4, 0.6, and 1C, respectively. The corresponding specific energy densities were 571, 520, 466, 417, and 357 Wh/kg, respectively (based on the total weight of SCC-SiG and NCM811). Fig. 7d depicts the extended cycling performance of the full cell at 0.2C charge and 0.4C discharge working conditions. The battery charge current density was kept at a lower current density of 0.2C to suppress any possibility of transition metal dissolution [58]. After 100 cycles, an area capacity of 0.823 mAh/cm^2 was retained, which corresponds to a capacity retention of 83%. The high capacity retention and indiscernible polarization growth (Fig. S7) indicate the reversible electrochemical reaction in SCC-SiG||NCM811 full cell. Further improvements are expected via optimizing the full cell with proper electrolyte/electrode formula and N/P ratio.

4. Conclusion

In summary, a series of Si-graphitic carbon (SiG) hybrids with various surface moieties were synthesized and comparatively studied as lithium-ion battery anodes. Featuring uniform embedment of Si nanoparticles in between expanded graphene layers, SiG material displays differing lithium cycling performance with respect to its tuned surface groups. In comparison with the carbon-coating, we found that a "sticky" carbon coating, i.e. epoxy-silane moieties attached to the carbon coating layer, gives rise to superior SEI stability and improved capacity retention.

These profound impacts were examined at high mass loading electrodes and full cells. The sticky carbon-coated SiG (SCC-SiG) demonstrates stable performances in high-area capacity half cells and full cells. Electrode mud-cracking and disintegration were inhibited by the aprotic "sticky" surface coating. Post-cycled electrode analysis identified a fluoro-polymer-rich SEI that may be exceptionally favorable with respect to conventional SEI components. A novel conclusion emerged is that aprotic "sticky" surface groups are the unrecognized key for Si-based anodes. We believe that the unraveled critical role of surface chemistry in determining cycle performances sheds light on the rational design of Si-based anodes for commercial LIBs applications.

CRediT authorship contribution statement

Zidong Chen: Methodology, Formal analysis, Visualization, Writing – original draft. **Lun Li:** Investigation, Formal analysis. **Zheng Zhang:** Investigation. **Hao Li:** Investigation. **Bo Xie:** Resources. **Yungui Chen:** Resources. **Ali Davoodi:** Formal analysis, Writing – review & editing. **Saman Hosseinpour:** Writing – review & editing. **Wei Liu:** Conceptualization, Writing – review & editing, Supervision, Funding acquisition.

Declaration of competing interest

The authors declare that they have no known competing financial interests or personal relationships that could have appeared to influence the work reported in this paper.

Acknowledgments

The authors acknowledge financial support from the National Natural Science Foundation of China (51702223), Collaborative Research Project of Chengdu (2019-GH02-00031-HZ), and SCU Postdoctoral Interdisciplinary Innovation Fund (0060304153008). The Authors thank Shanlin Wang, Hui Wang, and Yingming Zhu in the Analytical & Testing Center and INELT of SCU for their assistance in electron microscopy. S.H. thanks Prof. W. Peukert for supporting his research.

Appendix A. Supplementary data

Supplementary data to this article can be found online at https://doi.org/10.1016/j.carbon.2021.07.097.

References

[1] M. Armand, J.M. Tarascon, Building better batteries, Nature 451 (2008) 652–657.
[2] A. Franco Gonzalez, N.-H. Yang, R.-S. Liu, Silicon anode design for lithium-ion batteries: progress and perspectives, J. Phys. Chem. C 121 (2017) 27775–27787.
[3] S. Li, Y.-M. Liu, Y.-C. Zhang, Y. Song, G.-K. Wang, Y.-X. Liu, Z.-G. Wu, B.-H. Zhong, Y.-J. Zhong, X.-D. Guo, A review of rational design and investigation of binders applied in silicon-based anodes for lithium-ion batteries, J. Power Sources 485 (2021) 229331.
[4] M. Yuan, X. Guo, Y. Liu, H. Pang, Si-based materials derived from biomass: synthesis and applications in electrochemical energy storage, J. Mater. Chem. 7 (2019) 22123–22147.
[5] Z. Zheng, H.-H. Wu, H. Liu, Q. Zhang, X. He, S. Yu, V. Petrova, J. Feng, R. Kostecki, P. Liu, D.-L. Peng, M. Liu, M.-S. Wang, Achieving fast and durable lithium storage through amorphous FeP nanoparticles encapsulated in ultra-thin 3D P-doped porous carbon nanosheets, ACS Nano 14 (2020) 9545–9561.
[6] M. Dirican, M. Yanilmaz, K. Fu, O. Yildiz, H. Kizil, Y. Hu, X.W. Zhang, Carbon-confined PVA-derived silicon/silica/carbon nanofiber composites as anode for lithium-ion batteries, J. Electrochem. Soc. 161 (2014) A2197–A2203.
[7] X.R. Wu, C.H. Yu, C.C. Li, Carbon-encapsulated gigaporous microsphere as potential Si anode-active material for lithium-ion batteries, Carbon 160 (2020) 255–264.
[8] P.X. Jiang, Y.F. Liao, W. Liu, Y.G. Chen, Alternating nanolayers as lithiophilic scaffolds for Li-metal anode, J. Energy Chem. 57 (2021) 131–139.
[9] M. Ko, S. Chae, S. Jeong, P. Oh, J. Cho, Elastic a-silicon nanoparticle backboned graphene hybrid as a self-compacting anode for high-rate lithium ion batteries, ACS Nano 8 (2014) 8591–8599.
[10] C. Yao, X.L. Li, Y.X. Deng, Y.J. Li, P. Yang, S. Zhang, J. Yuan, R.H. Wang, An efficient prelithiation of graphene oxide nanoribbons wrapping silicon nanoparticles for stable Li+ storage, Carbon 168 (2020) 392–403.
[11] W. Liu, H. Li, J. Jin, Y. Wang, Z. Zhang, Z. Chen, Q. Wang, Y. Chen, E. Paek,

D. Mitlin, Synergy of epoxy chemical tethers and defect-free graphene in enabling stable lithium cycling of silicon nanoparticles, Angew. Chem. Int. Ed. 58 (2019) 16590–16600.
[12] Y. Li, K. Yan, H.-W. Lee, Z. Lu, N. Liu, Y. Cui, Growth of conformal graphene cages on micrometre-sized silicon particles as stable battery anodes, Nat. Energy 1 (2016) 15029.
[13] S. Kim, Y.K. Jeong, Y. Wang, H. Lee, J.W. Choi, A "sticky" mucin-inspired DNA-polysaccharide binder for silicon and silicon–graphite blended anodes in lithium-ion batteries, Adv. Mater. 30 (2018) 1707594.
[14] J. Ryu, S. Kim, J. Kim, S. Park, S. Lee, S. Yoo, J. Kim, N.S. Choi, J.H. Ryu, S. Park, Room-temperature crosslinkable natural polymer binder for high-rate and stable silicon anodes, Adv. Funct. Mater. 30 (2020) 1908433.
[15] X.Y. He, R. Han, P.X. Jiang, Y.G. Chen, W. Liu, Molecularly engineered conductive polymer binder enables stable lithium storage of Si, Ind. Eng. Chem. Res. 59 (2020) 2680–2688.
[16] C.-H. Jung, K.-H. Kim, S.-H. Hong, An in situ formed graphene oxide–polyacrylic acid composite cage on silicon microparticles for lithium ion batteries via an esterification reaction, J. Mater. Chem. 7 (2019) 12763–12772.
[17] H. Xu, Y. Wang, R. Chen, Y.L. Bai, T. Li, H. Jin, J.P. Wang, H.Y. Xia, A green-synthetic spiderweb-like Si@Graphene-oxide anode material with multi-functional citric acid binder for high energy-density Li-ion batteries, Carbon 157 (2020) 330–339.
[18] J. Li, D.-B. Le, P.P. Ferguson, J.R. Dahn, Lithium polyacrylate as a binder for tin–cobalt–carbon negative electrodes in lithium-ion batteries, Electrochim. Acta 55 (2010) 2991–2995.
[19] J.L. Gomez-Camer, C. Bunzli, M.M. Hantel, T. Poux, P. Novak, On the correlation between electrode expansion and cycling stability of graphite/Si electrodes for Li-ion batteries, Carbon 105 (2016) 42–51.
[20] I. Kovalenko, B. Zdyrko, A. Magasinski, B. Hertzberg, Z. Milicev, R. Burtovyy, I. Luzinov, G. Yushin, A major constituent of Brown algae for use in high-capacity Li-ion batteries, Science 334 (2011) 75–79.
[21] C.L. Campion, W. Li, B.L. Lucht, Thermal decomposition of LiPF6-based electrolytes for lithium-ion batteries, J. Electrochem. Soc. 152 (2005) A2327–A2334.
[22] A. Guéguen, D. Streich, M. He, M. Mendez, F.F. Chesneau, P. Novák, E.J. Berg, Decomposition of LiPF6 in high energy lithium-ion batteries studied with online electrochemical mass spectrometry, J. Electrochem. Soc. 163 (2016) A1095–A1100.
[23] E. Peled, S. Menkin, Review—SEI: past, present and future, J. Electrochem. Soc. 164 (2017) A1703–A1719.
[24] R. Jung, M. Metzger, D. Haering, S. Solchenbach, C. Marino, N. Tsiouvaras, C. Stinner, H.A. Gasteiger, Consumption of fluoroethylene carbonate (FEC) on Si-C composite electrodes for Li-ion batteries, J. Electrochem. Soc. 163 (2016) A1705–A1716.
[25] N. Delpuech, D. Mazouzi, N. Dupré, P. Moreau, M. Cerbelaud, J.S. Bridel, J.C. Badot, E. De Vito, D. Guyomard, B. Lestriez, B. Humbert, Critical role of silicon nanoparticles surface on lithium cell electrochemical performance analyzed by FTIR, Raman, EELS, XPS, NMR, and BDS spectroscopies, J. Phys. Chem. C 118 (2014) 17318–17331.
[26] M. Leskes, G. Kim, T. Liu, A.L. Michan, F. Aussenac, P. Dorffer, S. Paul, C.P. Grey, Surface-sensitive NMR detection of the solid electrolyte interphase layer on reduced graphene oxide, J. Phys. Chem. Lett. 8 (2017) 1078–1085.
[27] R. Xu, R. Wei, X. Hu, Y. Li, L. Wang, K. Zhang, Y. Wang, H. Zhang, F. Liang, Y. Yao, A strategy and detailed explanations to the composites of Si/MWCNTs for lithium storage, Carbon 171 (2021) 265–275.
[28] A.M. Dimiev, G. Ceriotti, A. Metzger, N.D. Kim, J.M. Tour, Chemical mass production of graphene nanoplatelets in ~100% yield, ACS Nano 10 (2016) 274–279.
[29] S. Park, R.S. Ruoff, Chemical methods for the production of graphenes, Nat. Nanotechnol. 5 (2010), 309-309.
[30] K.H. Park, D. Lee, J. Kim, J. Song, Y.M. Lee, H.-T. Kim, J.-K. Park, Defect-free, size-tunable graphene for high-performance lithium ion battery, Nano Lett. 14 (2014) 4306–4313.
[31] P. Handel, G. Fauler, K. Kapper, M. Schmuck, C. Stangl, R. Fischer, F. Uhlig, S. Koller, Thermal aging of electrolytes used in lithium-ion batteries – an investigation of the impact of protic impurities and different housing materials, J. Power Sources 267 (2014) 255–259.
[32] S.-H. Choi, G. Nam, S. Chae, D. Kim, N. Kim, W.S. Kim, J. Ma, J. Sung, S.M. Han, M. Ko, H.-W. Lee, J. Cho, Robust pitch on silicon nanolayer–embedded graphite for suppressing undesirable volume expansion, Adv. Energy Mater. 9 (2019) 1803121.
[33] Y. Zeng, Y. Huang, N. Liu, X. Wang, Y. Zhang, Y. Guo, H.-H. Wu, H. Chen, X. Tang, Q. Zhang, N-doped porous carbon nanofibers sheathed pumpkin-like Si/C composites as free-standing anodes for lithium-ion batteries, J. Energy Chem. 54 (2021) 727–735.
[34] W. An, B. Gao, S. Mei, B. Xiang, J. Fu, L. Wang, Q. Zhang, P.K. Chu, K. Huo, Scalable synthesis of ant-nest-like bulk porous silicon for high-performance lithium-ion battery anodes, Nat. Commun. 10 (2019) 1447.
[35] Z. Yi, Y. Qian, C.H. Cao, N. Lin, Y.T. Qian, Porous Si/C microspheres decorated with stable outer carbon interphase and inner interpenetrated Si@C channels for enhanced lithium storage, Carbon 149 (2019) 664–671.
[36] R. Raccichini, A. Varzi, D. Wei, S. Passerini, Critical insight into the relentless progression toward graphene and graphene-containing materials for lithium-ion battery anodes, Adv. Mater. 29 (2016) 1603421.
[37] E.Y. Polyakova, K.T. Rim, D. Eom, K. Douglass, R.L. Opila, T.F. Heinz, A.V. Teplyakov, G.W. Flynn, Scanning tunneling microscopy and X-ray photoelectron spectroscopy studies of graphene films prepared by sonication-assisted dispersion, ACS Nano 5 (2011) 6102–6108.
[38] V.V. Kaichev, M. Morkel, H. Unterhalt, I.P. Prosvirin, V.I. Bukhtiyarov, G. Rupprechter, H.J. Freund, C–O bond scission on "defect-rich and perfect" Pd(111)? Surf. Sci. 566–568 (2004) 1024–1029.
[39] L. Jiang, R. Zou, W. Li, J. Sun, X. Hu, Y. Xue, G. He, J. Hu, Ni(OH)2/CoO/reduced graphene oxide composites with excellent electrochemical properties, J. Mater. Chem. 1 (2013) 478–481.
[40] Y. Ye, D. Zhang, T. Liu, Z. Liu, J. Pu, W. Liu, H. Zhao, X. Li, L. Wang, Superior corrosion resistance and self-healable epoxy coating pigmented with silanized trianiline-intercalated graphene, Carbon 142 (2019) 164–176.
[41] C. Tarducci, E.J. Kinmond, J.P.S. Badyal, S.A. Brewer, C. Willis, Epoxide-functionalized solid surfaces, Chem. Mater. 12 (2000) 1884–1889.
[42] W. Liu, Y. Xia, W. Wang, Y. Wang, J. Jin, Y. Chen, E. Paek, D. Mitlin, Pristine or highly defective? Understanding the role of graphene structure for stable lithium metal plating, Adv. Energy Mater. 9 (2019) 1802918.
[43] W. Yuan, Y. Zhou, Y. Li, C. Li, H. Peng, J. Zhang, Z. Liu, L. Dai, G. Shi, The edge- and basal-plane-specific electrochemistry of a single-layer graphene sheet, Sci. Rep. 3 (2013) 2248.
[44] X. Ma, J.E. Harlow, J. Li, L. Ma, D.S. Hall, S. Buteau, M. Genovese, M. Cormier, J.R. Dahn, Hindering rollover failure of Li[Ni0.5Mn0.3Co0.2]O2/graphite pouch cells during long-term cycling, J. Electrochem. Soc. 166 (2019) A711–A724.
[45] E. Markevich, G. Salitra, D. Aurbach, Fluoroethylene carbonate as an important component for the formation of an effective solid electrolyte interphase on anodes and cathodes for advanced Li-ion batteries, ACS Energy Lett 2 (2017) 1337–1345.
[46] R. Petibon, V.L. Chevrier, C.P. Aiken, D.S. Hall, S.R. Hyatt, R. Shunmugasundaram, J.R. Dahn, Studies of the capacity fade mechanisms of LiCoO2/Si-alloy: graphite cells, J. Electrochem. Soc. 163 (2016) A1146–A1156.
[47] D. Aurbach, B. Markovsky, A. Shechter, Y. Ein-Eli, H. Cohen, A comparative study of synthetic graphite and Li electrodes in electrolyte solutions based on ethylene carbonate-dimethyl carbonate mixtures, J. Electrochem. Soc. 143 (1996) 3809–3820.
[48] W. Liu, Z. Chen, Z. Zhang, P. Jiang, Y. Chen, E. Paek, Y. Wang, D. Mitlin, Lithium-activated SnS–graphene alternating nanolayers enable dendrite-free cycling of thin sodium metal anodes in carbonate electrolyte, Energy Environ. Sci. 14 (2021) 382–395.
[49] Y. Kamikawa, K. Amezawa, K. Terada, First-principles study on the mechanical properties of polymers formed by the electrochemical reduction of fluoroethylene carbonate and vinylene carbonate, J. Phys. Chem. C 124 (2020) 19937–19944.
[50] I.A. Shkrob, J.F. Wishart, D.P. Abraham, What makes fluoroethylene carbonate different? J. Phys. Chem. C 119 (2015) 14954–14964.
[51] H. Nakai, T. Kubota, A. Kita, A. Kawashima, Investigation of the solid electrolyte interphase formed by fluoroethylene carbonate on Si electrodes, J. Electrochem. Soc. 158 (2011) A798.
[52] V. Etacheri, O. Haik, Y. Goffer, G.A. Roberts, I.C. Stefan, R. Fasching, D. Aurbach, Effect of fluoroethylene carbonate (FEC) on the performance and surface chemistry of Si-nanowire Li-ion battery anodes, Langmuir 28 (2012) 965–976.
[53] C.-H. Jung, K.-H. Kim, S.-H. Hong, Stable silicon anode for lithium-ion batteries through covalent bond formation with a binder via esterification, ACS Appl. Mater. Interfaces 11 (2019) 26753–26763.
[54] Q. Yun, X. Qin, W. Lv, Y.-B. He, B. Li, F. Kang, Q.-H. Yang, "Concrete" inspired construction of a silicon/carbon hybrid electrode for high performance lithium ion battery, Carbon 93 (2015) 59–67.
[55] Y. Chen, Y. Lin, N. Du, Y. Zhang, H. Zhang, D. Yang, A critical SiOx layer on Si porous structures to construct highly-reversible anode materials for lithium-ion batteries, Chem. Commun. 53 (2017) 6101–6104.
[56] H.J. Kim, S. Choi, S.J. Lee, M.W. Seo, J.G. Lee, E. Deniz, Y.J. Lee, E.K. Kim, J.W. Choi, Controlled prelithiation of silicon monoxide for high performance lithium-ion rechargeable full cells, Nano Lett. 16 (2016) 282–288.
[57] A. Kajiyama, K. Takada, T. Inada, M. Kouguchi, S. Kondo, M. Watanabe, Layered Li-Co-Mn oxide as a high-voltage positive electrode material for lithium batteries, J. Electrochem. Soc. 148 (2001) A981–A983.
[58] C. Zhan, T. Wu, J. Lu, K. Amine, Dissolution, migration, and deposition of transition metal ions in Li-ion batteries exemplified by Mn-based cathodes – a critical review, Energy Environ. Sci. 11 (2018) 243–257.